Origin of Inverse Emission Behaviour in Strain-engineered Zero-Dimensional Tin Halides: All-inorganic vs. Hybrid

Dhritismita Sarma, Palak Chugh, Anshid Kuttasseri, Arup Mahata*

Department of Chemistry, Indian Institute of Technology Hyderabad, Kandi, Sangareddy, 502284, Telangana, India

Email: arup@chy.iith.ac.in (A.M.)

Contents:

Figure S13. Planar average charge density distribution of electron and hole and their overlap at the critical pressure range ((6% and 7% strain) (a,b) Cs_4SnBr_4 and (c,d) $(C_9NH_{20})_2SnBr_4$.

Figure S14. Analysis of spin asymmetry associated with the spin 1 HOMO-1 state in the PDOS of $(C_9NH_{20})_2SnBr_4$.

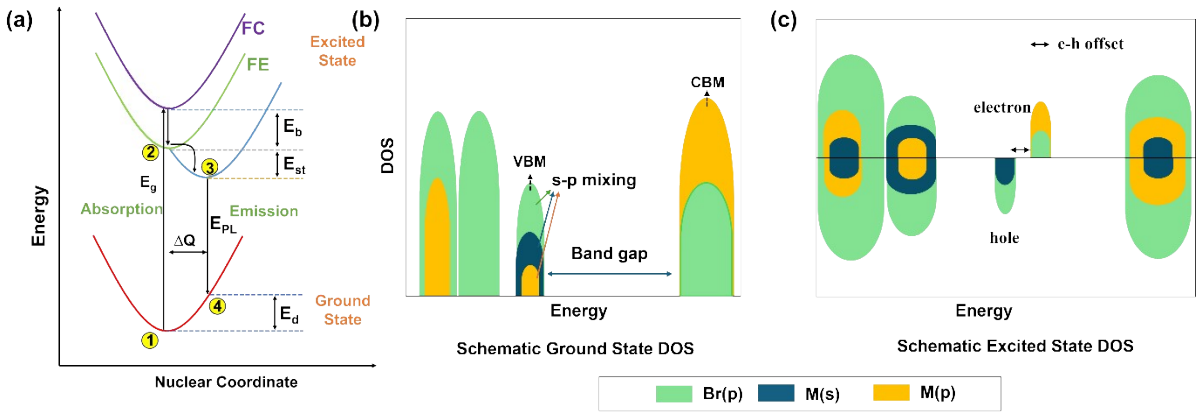

Figure S1. (a) Δ SCF method used in our study showing schematic configuration coordinate diagram used to evaluate ground- and excited-state descriptors and schematic (b) ground and (c) excited state DOS showing s-p mixing at the VBM and electron-hole offset.

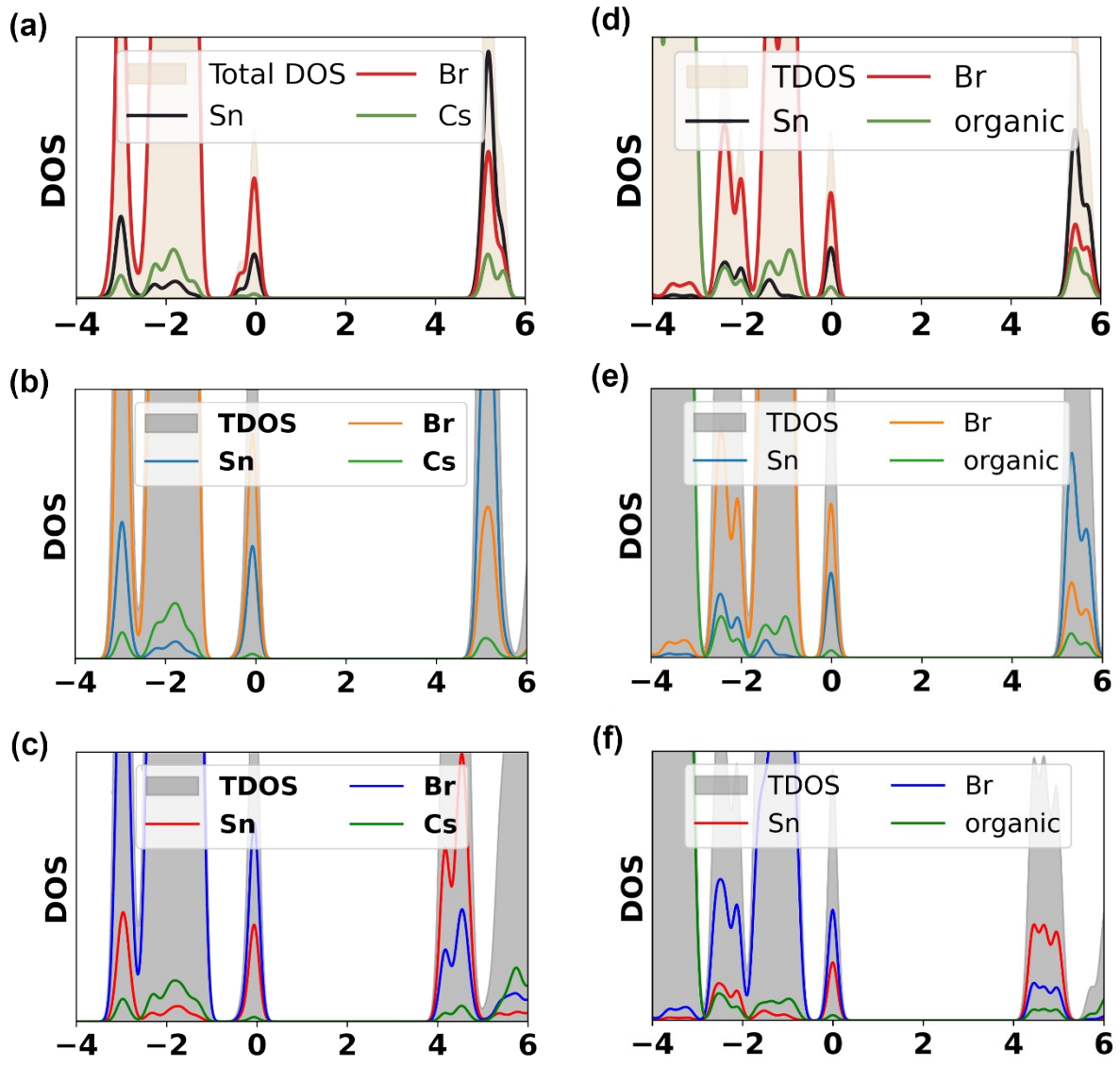

Figure S2. Comparison of the band edges distribution of PBE0+25% HF in CP2K, PBE0+25% HF in VASP and HSE+SOC+ 25% HF in VASP for (a,b,c) Cs_4SnBr_4 and (d,e,f) $(C_9NH_{20})_2SnBr_4$. Since our analysis focuses on relative energetic separations and band-edge alignment to interpret ground- and excited-state photophysical behaviour, methodological consistency was maintained within the CP2K framework. Due to the limitation of SOC in CP2K we have performed our calculations in the PBE0 with 25% HF hybrid level of theory. Although PBE0 slightly overestimates absolute band gaps, it provides a consistent hybrid-level description for both ground- and excited-state configurations; therefore, only hybrid-level DOS results are presented to avoid artifacts arising from mixing different levels of theory.

Text S1. Ground- and Excited-State Electronic Structure Analysis

Figure S1 presents the schematic ground-and excited-state DOS used to rationalize the photophysical behaviour. In ns^2 metal halides, the CB mainly arises from hybridized metal p and halide p orbitals. The VB comprises multiple components: VBM is dominated by an antibonding metal s and halide p orbital, followed by nonbonding halide p states, deeper bonding metal p and halide p states, and finally a low-energy bonding metal s and halide p state. The metal p contribution within the antibonding state reflects s-p mixing, indicative of lone-pair stereochemical activity. Enhanced lone-pair exposure increases lattice repulsion, promoting structural distortions that further strengthen s–p mixing.[3,4]

Upon excitation, an electron is promoted to a CB state composed of metal p and halide p antibonding orbitals, leaving a hole in the metal ns^2 and halide p antibonding valence state. Excited-state lattice relaxation lowers the energy of the electron-localized CB (electron-state stabilization) while modifying the energy of the hole-localized state VB (hole-state destabilization). The electron subsequently localizes near the hole, bound by exciton binding energy, leading to self-trapped exciton (STE) formation. Greater electron-hole localization enhances STE stabilization, and the cumulative effect of the electron-state stabilization and hole-state destabilization manifests as an increased Stokes shift.

Text S2. Excited state parameter.[1,2]

In the context of exciton self-trapping and emission, several key physical descriptors emerge from the coordination configuration diagram (CCD) (Figure S1), which are associated with the excited-state relaxation process:

- **E_{st} = Self Trapped Exciton Energy:** This energy corresponds to the stabilization obtained when a free exciton localizes leading to the formation of a self-trapped exciton (STE). In our study, the STE is described within the triplet excited-state framework. It is defined as the triplet relaxation and corresponds to the energy difference between point 2 and point 3.
- **E_d = Lattice Deformation Energy:** Once the STE is stabilized at its excited-state minimum, it undergoes a vertical transition to a vibrationally higher energy state on the ground-state potential energy surface. Because this transition occurs without structural relaxation, the system is placed in a distorted geometry on the ground-state surface, resulting in an increase in ground-state energy. Here, in our model the energy difference between point 4 and point 1.
- **E_{PL} = Emission Energy:** This corresponds to the radiative emission energy released when the self-trapped exciton returns to the ground state. It is given by the energy difference between point 3 and point 4.
- **ΔQ= Mass-weighted displacement:** The formation of the STE is accompanied by significant lattice distortion. This parameter corresponds to the mass-weighted displacement between the relaxed free-exciton geometry and the STE geometry, providing a quantitative measure of the structural reorganization involved in self-trapping. Mathematically:

$$\left[\sum_{\alpha=1}^{N_{atom}} \sum_{i=x,y,z} M_\alpha (R_{\alpha i}^{ES} - R_{\alpha i}^{GS})^2\right]^{1/2}$$

where M_α is the mass of the α^{th} atom, and $R_{\alpha i}^{GS}$ ($R_{\alpha i}^{ES}$) is the atomic coordinate of the α^{th} atom in the i^{th} direction of the GS (ES).

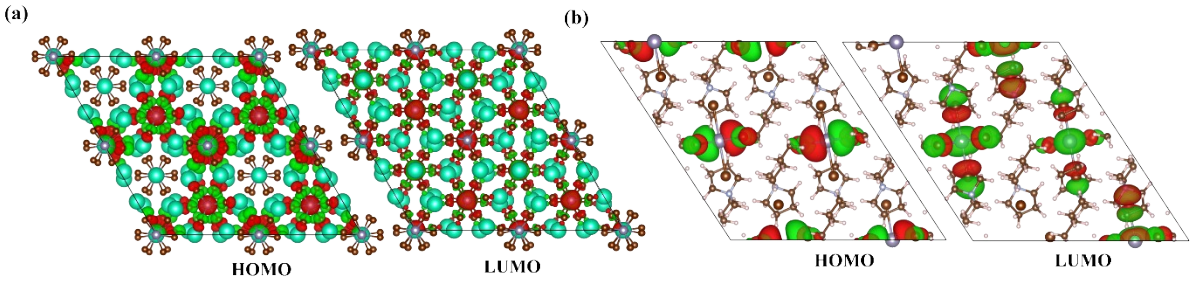

Figure S3. Ground state band edge charge density localization of (a) Cs_4SnBr_4 and (b) $(C_9NH_{20})_2SnBr_4$

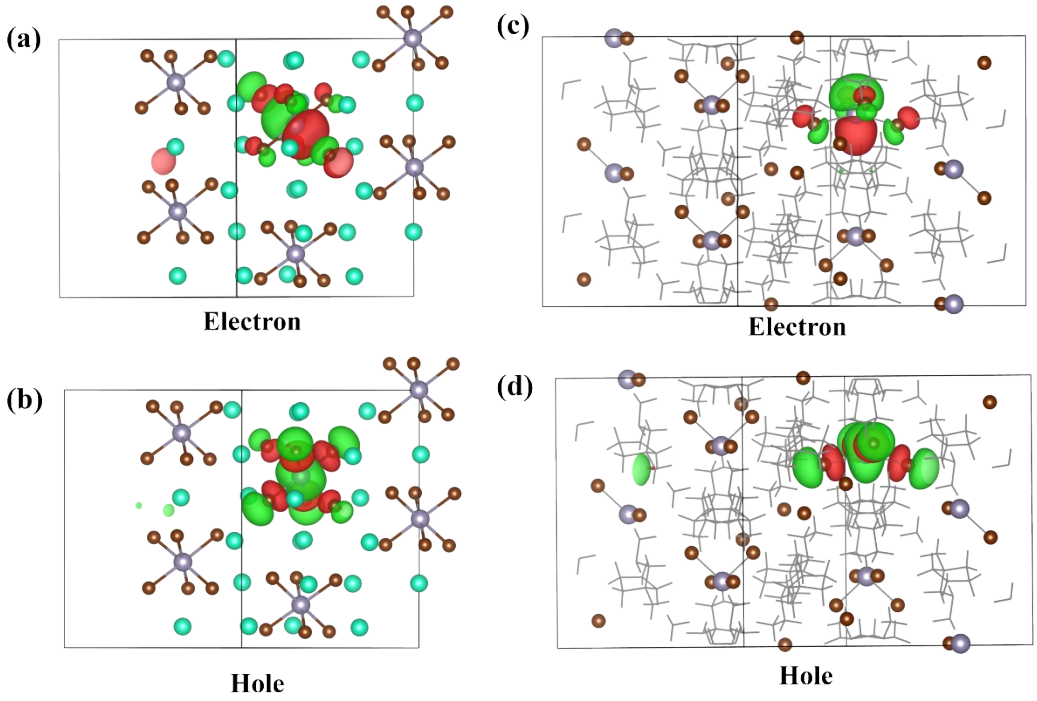

Figure S4. Excited state Kohn Sham orbitals of electron and hole of (a,b) Cs_4SnBr_4 and (c,d) $(C_9NH_{20})_2SnBr_4$ at 0% pressure.

Table S1. Standardization of the band gap of the Cs_4SnBr_4 and $(C_9NH_{20})_2SnBr_4$ systems with different levels of theory to match the experimental bulk.

	VASP		CP2K	
System	HSE06-25% HF + SOC (eV)	PBE0-25% HF (eV)	PBE0-25% HF (eV)	Experimental band gap (eV)
Cs_4SnBr_4	4.06	4.81	4.76	3.38[5]
$(C_9NH_{20})_2SnBr_4$	4.38	5.20	5.31	3.45[6]

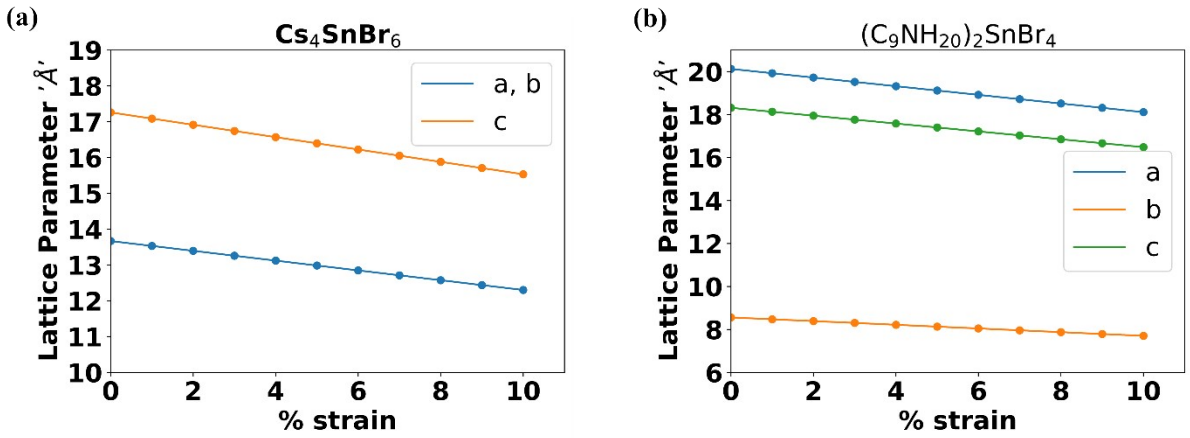

Figure S5. Evolution of Lattice parameters of (a) Cs_4SnBr_4 and (b) $(C_9NH_{20})_2SnBr_4$.

Table S2. The structural and electronic parameters of the geometry-optimized unit cell for Cs_4SnBr_4 and $(C_9NH_{20})_2SnBr_4$.

System	Compression %	Lattice parameter (Å)		Volume (Å^3)	Average bond length (Å)		Band Gap (eV)	Smallest Distance (Å)	
		a	c		Axial	Equatorial		Sn-Sn	Br-Br
Cs_4SnBr_6	Pristine	13.67	17.26	2792.66	3.00	3.00	4.99	8.38	4.02
	1%	13.53	17.09	2709.72	3.00	3.00	4.95	8.32	3.99
	2%	13.40	16.91	2628.43	2.99	2.99	4.90	8.23	3.93
	3%	13.26	16.74	2548.79	2.98	2.98	4.86	8.15	3.88
	4%	13.12	16.57	2470.77	2.97	2.97	4.81	8.06	3.82
	5%	12.99	16.40	2394.36	2.96	2.96	4.76	7.98	3.77
	6%	12.85	16.22	2319.54	2.95	2.95	4.70	7.90	3.72
	7%	12.71	16.05	2246.30	2.97	3.09	4.06	7.81	3.37
	8%	12.58	15.88	2174.61	2.93	2.93	3.92	7.72	3.30
	9%	12.44	15.71	2104.47	2.92	2.92	3.81	7.64	3.23
	10%	12.30	15.53	2035.85	2.91	2.91	3.70	7.56	3.17

System	Compression %	Lattice parameter (Å)			Volume (Å^3)	Average bond length (Å)		Band Gap (eV)	Smallest Distance (Å)	
		a	b	c		Axial	Equatorial		Sn-Sn	Br-Br
$(C_9NH_{20})_2SnBr_4$	Pristine	20.12	8.56	18.31	2635.88	2.70	3.03	5.31	8.56	6.17
	1%	19.92	8.47	18.13	2557.60	2.70	3.02	5.29	8.47	6.08
	2%	19.72	8.39	17.95	2480.87	2.70	3.00	5.31	8.39	6.01
	3%	19.52	8.30	17.76	2405.70	2.69	2.98	5.31	8.30	5.90
	4%	19.32	8.22	17.58	2332.06	2.69	2.96	5.30	8.22	5.79
	5%	19.12	8.13	17.40	2259.94	2.69	2.94	5.29	8.13	5.68
	6%	18.92	8.05	17.22	2189.32	2.68	2.92	5.29	8.05	5.55
	7%	18.72	7.96	17.03	2120.19	2.68	2.91	5.27	7.96	5.49
	8%	18.51	7.87	16.85	2052.53	2.67	2.89	5.28	7.87	5.51
	9%	18.31	7.79	16.67	1986.33	2.66	2.88	5.25	7.79	5.45
	10%	18.11	7.70	16.48	1921.56	2.65	2.86	5.23	7.70	5.38

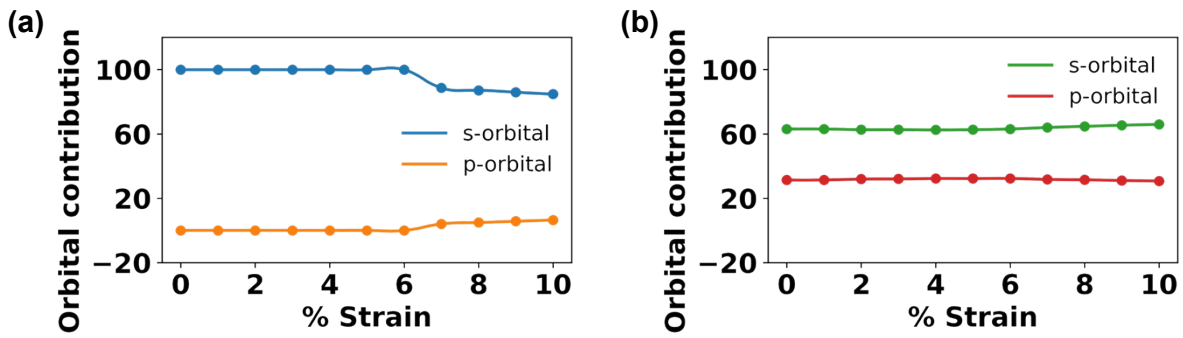

Figure S6. Metal s-p orbital contribution at the top VBM of (a) Cs_4SnBr_4 and (b) $(C_9NH_{20})_2SnBr_4$.

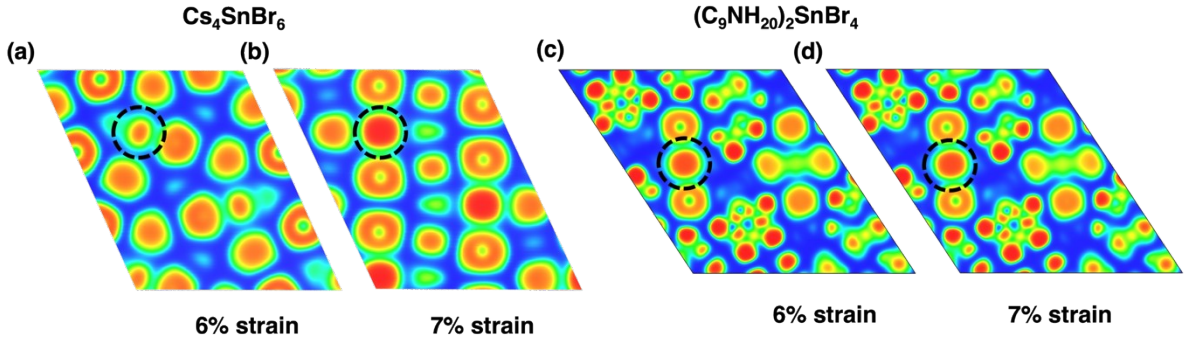

Figure S7. ELF maps of (a,b) Cs_4SnBr_6 and (c,d) $(C_9NH_{20})_2SnBr_4$ under 6% and 7% compression. The dotted circle highlights the Sn center.

Text S3. Band-Edge Alignment.

In periodic bulk structures, the absence of an explicit vacuum region prevents the direct alignment of electronic energies to an absolute vacuum level. Under these constraints, the bulk band edges were aligned with respect to the deepest occupied Kohn-Sham state, providing a consistent internal reference for comparative band alignment across different compositions. This procedure is well established in the literature and has been widely adopted in previous theoretical studies for bulk electronic energy alignment.[7,8]

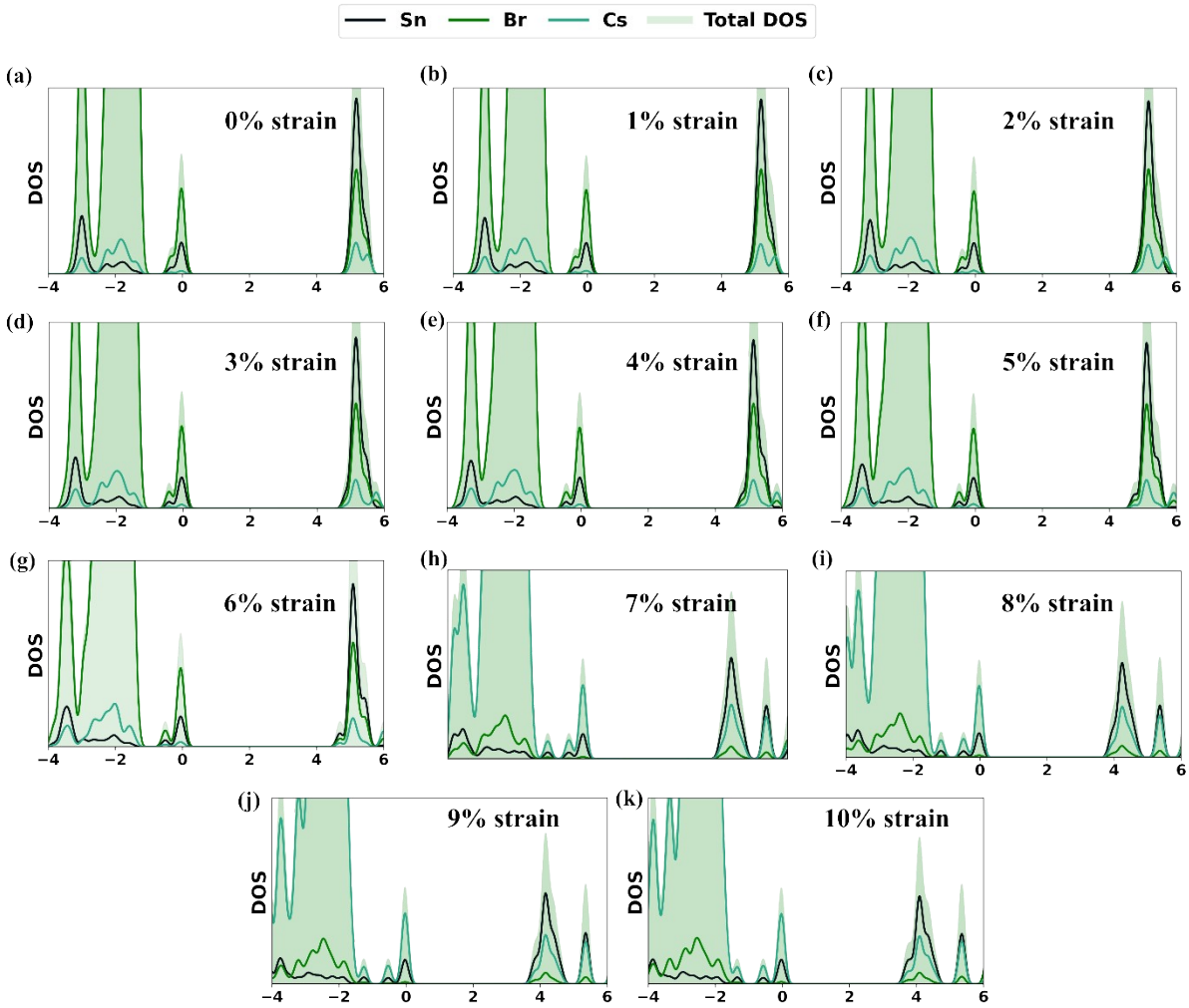

Figure S8. Partial density of state for Cs_4SnBr_6 structure from pristine to 10%.

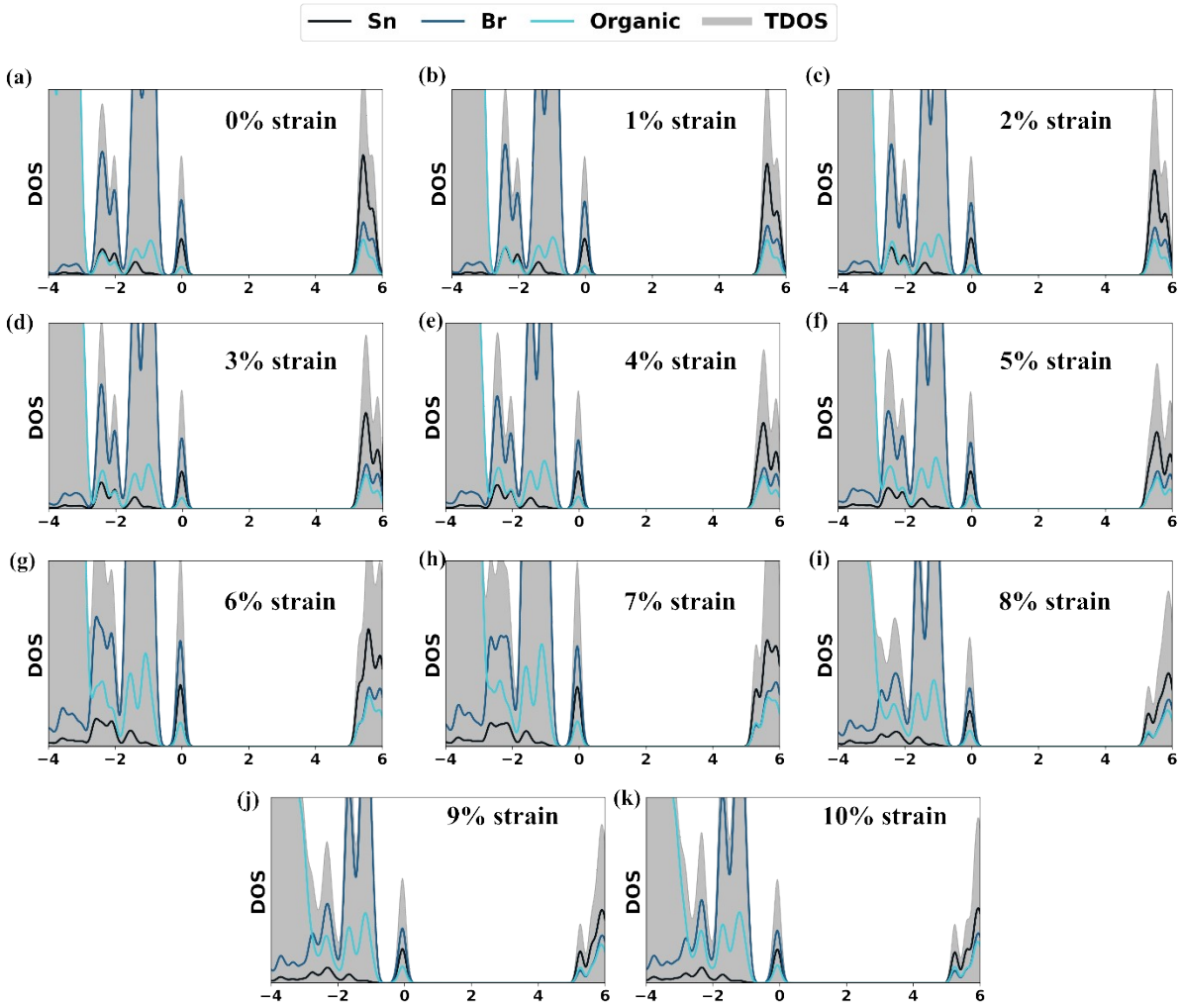

Figure S9. Partial density of state for $(C_9NH_{20})_2SnBr_4$ hybrid structure from pristine to 10%.

Table S3. Excited state parameter for Cs_4SnBr_4 and $(C_9NH_{20})_2SnBr_4$ using Δ SCF model.

System	Compression %	E_{st} (eV)	E_d (eV)	ΔQ (ÅAMU$^{1/2}$)	E_{PL} (eV)	$E_{st}+E_d$ (eV)
Cs_4SnBr_6	Pristine	0.70	0.76	11.24	2.32	1.46
	1%	0.66	0.74	10.92	2.34	1.41
	2%	0.69	0.73	10.93	2.36	1.43
	3%	0.62	0.72	10.69	2.38	1.34
	4%	0.60	0.71	10.92	2.38	1.32
	5%	0.59	0.71	11.84	2.36	1.31
	6%	0.59	0.74	14.18	2.31	1.34
	7%	0.84	0.71	14.69	1.49	1.55
	8%	0.81	0.69	12.79	1.46	1.50
	9%	0.79	0.68	12.24	1.42	1.47
	10%	0.77	0.68	11.83	1.37	1.45

System	Compression %	E_{st} (eV)	E_d (eV)	ΔQ (ÅAMU$^{1/2}$)	E_{PL} (eV)	E_{st}+E_d (eV)
$(C_9NH_{20})_2SnBr_4$	Pristine	1.15	0.94	14.70	1.66	2.09
	1%	1.10	0.99	14.73	1.66	2.09
	2%	1.07	1.04	14.52	1.63	2.11
	3%	1.05	1.09	14.88	1.59	2.14
	4%	1.01	1.12	14.51	1.60	2.13
	5%	0.98	1.16	14.53	1.59	2.14
	6%	0.85	1.27	13.67	1.61	2.11
	7%	0.48	0.60	8.05	2.65	1.09
	8%	0.44	0.56	6.84	2.74	1.00
	9%	0.43	0.55	7.79	2.75	0.99
	10%	0.42	0.55	7.71	2.78	0.96

Table S4. Excited state structural parameters for Cs_4SnBr_4 and $(C_9NH_{20})_2SnBr_4$ under compression.

System	Compression %	Average Triplet Bond length (Å)		Smallest Distance (Å)	
		Axial	Equatorial	Sn-Sn	Br-Br
Cs_4SnBr_6	Pristine	3.51	2.82	8.29	3.87
	1%	3.51	2.82	8.26	3.87
	2%	3.48	2.82	8.18	3.81
	3%	3.45	2.97	8.10	3.75
	4%	3.43	2.81	8.02	3.69
	5%	3.41	2.80	7.93	3.63
	6%	3.40	2.80	7.85	3.56
	7%	3.74	2.84	7.75	3.33
	8%	3.70	2.83	7.67	3.26
	9%	3.68	2.83	7.59	3.20
	10%	3.65	2.83	7.50	3.14

System	Compression %	Average Triplet Bond length (Å)		Smallest Distance (Å)	
$(C_9NH_{20})_2SnBr_4$		Axial	Equatorial	Sn-Sn	Br-Br
	Pristine	2.74	2.88	7.77	5.47
	1%	2.74	2.87	7.65	5.40
	2%	2.73	2.86	7.55	5.31
	3%	2.72	2.84	7.45	5.17
	4%	2.71	2.83	7.37	5.09
	5%	2.70	2.81	7.30	4.96
	6%	2.69	2.80	7.19	4.89
	7%	2.67	2.92	7.75	5.42
	8%	2.66	2.88	7.70	5.33
	9%	2.65	2.86	7.62	5.25
	10%	2.66	2.86	7.70	5.38

Text S4. Singlet vs Triplet STE

To evaluate the possibility of singlet-triplet interconversion, we have modelled the free exciton (FE) state within the ΔSCF framework and estimated the combined energetic barrier $E_{\text{barrier}} = E_{\text{st}} + E_b$, where E_{st} is the STE relaxation energy and E_b is the exciton binding energy calculated by $E_b = E(\text{Singlet}) + E_g - E(\text{FE})$ (Figure S1). For Cs_4SnBr_6, the calculated barriers at 6% and 7% compression (the critical pressure range) are 1.64 eV and 1.86 eV, respectively, while for $(C_9NH_{20})_2SnBr_4$ the corresponding values are 2.66 eV and 2.53 eV. These barriers are substantially larger than thermal energies at ambient conditions, rendering reverse relaxation from the triplet STE to a singlet configuration energetically unfavorable. Therefore, emission is expected to proceed predominantly from the triplet centre, with negligible probability of interconversion back to a singlet emissive state.

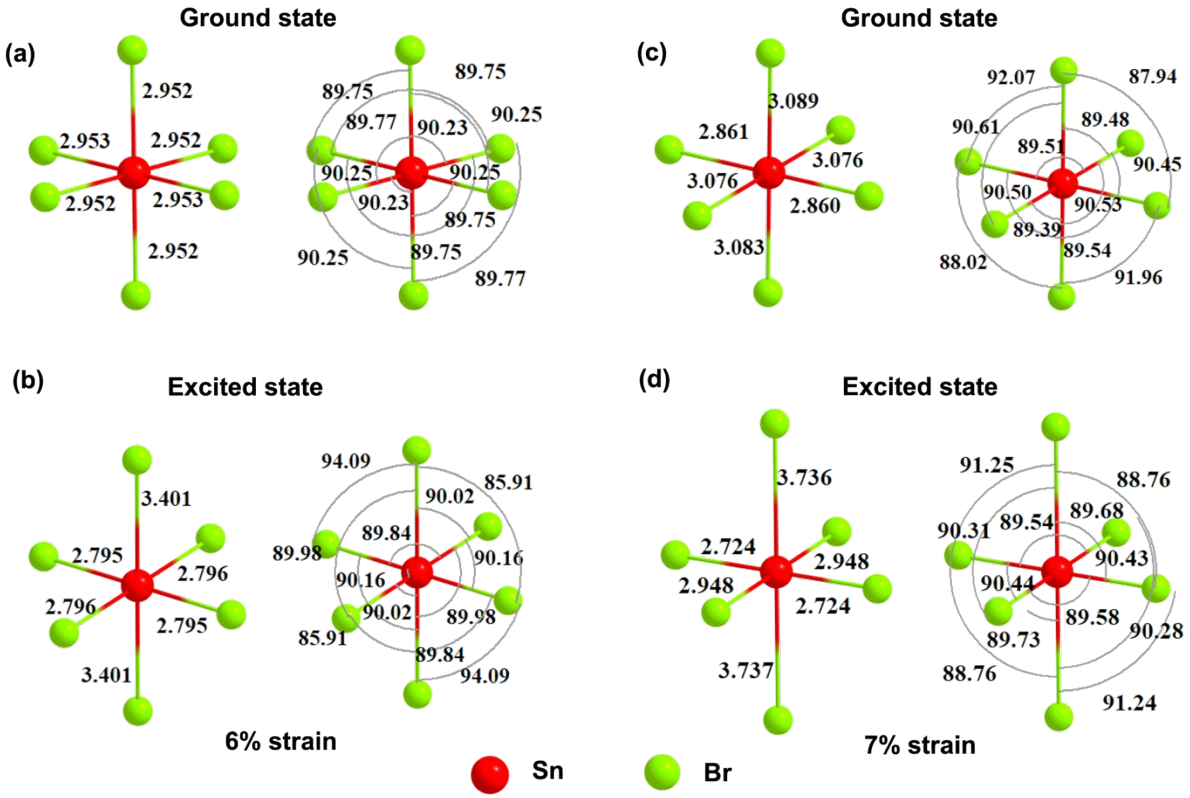

Figure S10. Bond length and bond angle distribution at ground and excited state for Cs_4SnBr_4 at the critical pressure range (a,b) 6% strain and (c,d) 7% strain.

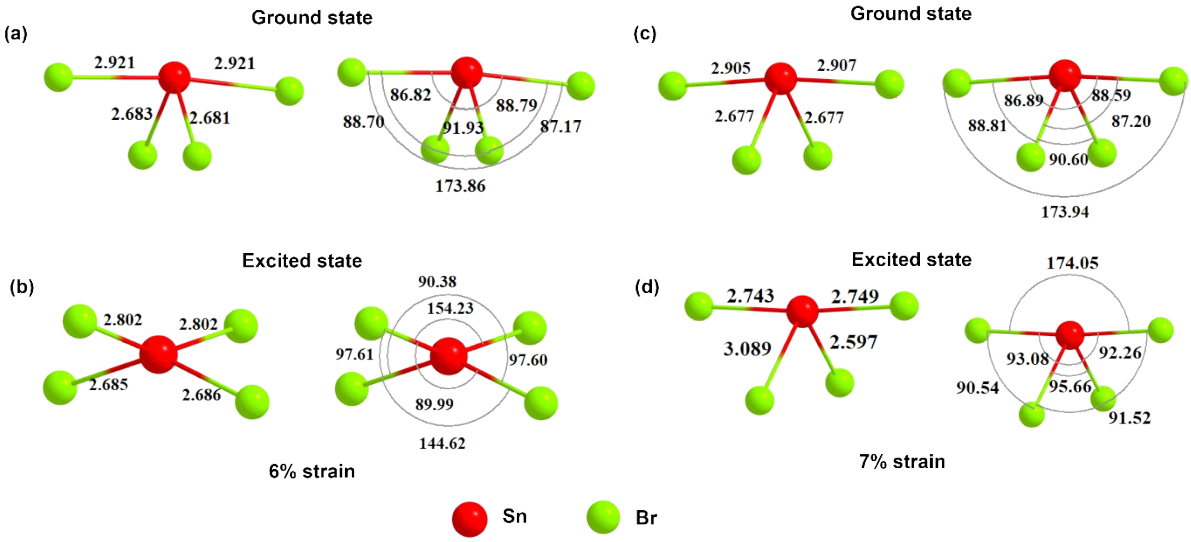

Figure S11. Bond length and bond angle distribution at ground and excited state for $(C_9NH_{20})_2SnBr_4$ at the critical pressure range (a,b) 6% strain and (c,d) 7% strain.

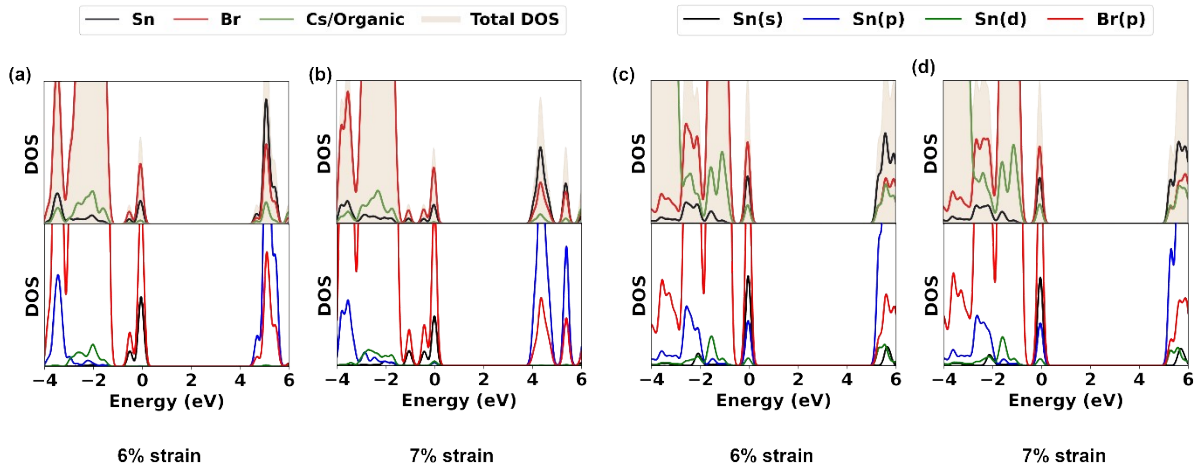

Figure S12. Ground state atomic PDOS (upper panel) and orbital resolved PDOS the critical pressure range ((6% and 7% strain) (a,b) Cs_4SnBr_4 and (c,d) $(C_9NH_{20})_2SnBr_4$.

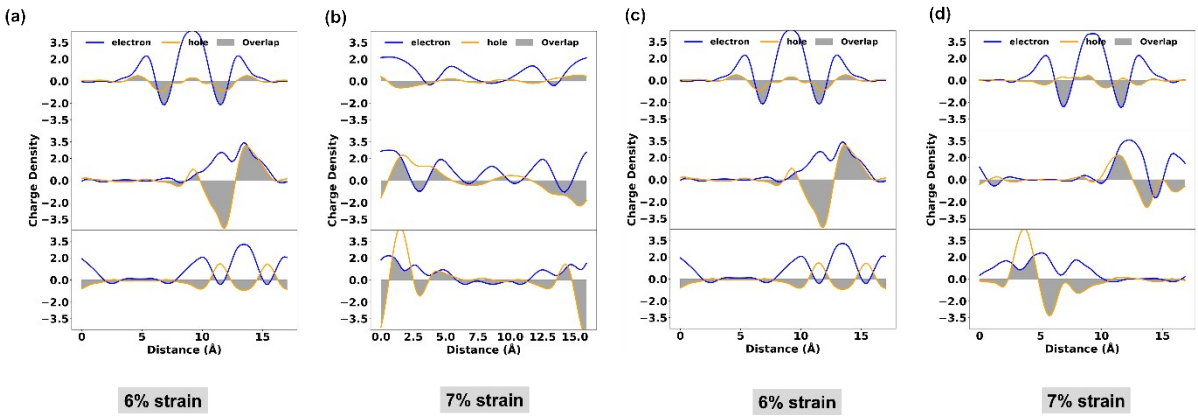

Figure S13. Planar average charge density distribution of electron and hole and their overlap at the critical pressure range ((6% and 7% strain) (a,b) Cs_4SnBr_4 and (c,d) $(C_9NH_{20})_2SnBr_4$.

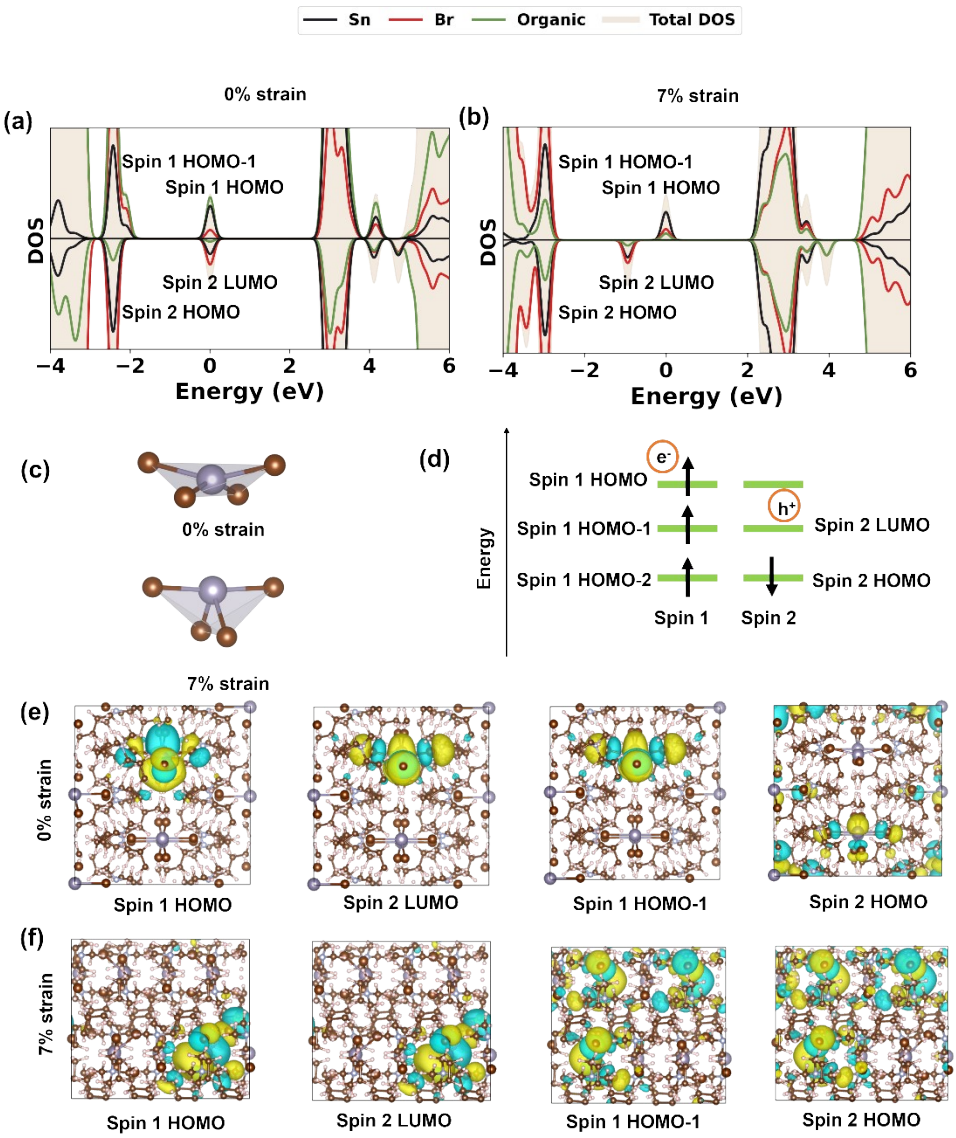

Figure S14. Analysis of spin asymmetry associated with the spin 1 HOMO-1 state in the PDOS of $(C_9NH_{20})_2SnBr_4$. PDOS at(a) 0% where spin asymmetry is present and (b) 7% where no asymmetry present; (c) structural evolution of the configuration corresponding spin 1 HOMO-1 from 0-7%; (d) Schematic illustration of the spin-channel representation used in the DOS plots; Kohn sham orbitals of $(C_9NH_{20})_2SnBr_4$ for (e) 0% and (f) 7% compression. The observed PDOS asymmetry originates from compression-induced structural distortion and symmetry breaking leading to a orbital rehybridization, which lifts the near-degeneracy between spin-1 HOMO−1 and spin-2 HOMO in the disphenoidal system. At higher compression (7%), the ground and excited state structural symmetry enhances orbital delocalization, thereby eliminating the apparent spin asymmetry.

Reference:

1 S. Li, J. Luo, J. Liu and J. Tang, *J. Phys. Chem. Lett.*, 2019, **10**, 1999–2007.
2 J. Gavnholt, T. Olsen, M. Engelund and J. Schiøtz, *Phys. Rev. B*, 2008, **78**, 075441.
3 V. Morad, S. Yakunin and M. V. Kovalenko, *ACS Materials Lett.*, 2020, **2**, 845–852.
4 A. Vogler and H. Nikol, *Comments on Inorganic Chemistry*, DOI:10.1080/02603599308048663.
5 R. H. Andrews, S. J. Clark, J. D. Donaldson, J. C. Dewan and J. Silver, *J. Chem. Soc., Dalton Trans.*, 1983, 767–770.
6 C. Zhou, H. Lin, H. Shi, Y. Tian, C. Pak, M. Shatruk, Y. Zhou, P. Djurovich, M.-H. Du and B. Ma, *Angewandte Chemie International Edition*, 2018, **57**, 1021–1024.
7 M. Coduri, T. B. Shiell, T. A. Strobel, A. Mahata, F. Cova, E. Mosconi, F. D. Angelis and L. Malavasi, *Mater. Adv.*, 2020, **1**, 2840–2845.
8 R. Das, D. Swain, A. Mahata, D. Prajapat, S. K. Upadhyay, S. Saikia, V. R. Reddy, F. De Angelis and D. D. Sarma, *Chem. Mater.*, 2024, **36**, 1891–1898.